Numerical Study of Flow Augmented Thermal Management for Entry and Re-entry Environments

Gary C. Cheng*, Kshitij D. Neroorkar†, Yen-Sen Chen‡, Ten-See Wang§, and Endwell O. Daso**

Abstract

Tremendous amounts of heat and drag loads occur during entry and re-entry into planetary and earth atmospheres have posed grave challenges on maintaining structure integrity of space exploration vehicles. Though various thermal protection systems (TPS) have been employed to manage the heat loads, both localized and transient spikes at stagnation points, the use of TPS can substantially increase the weight of the vehicle. Hence, various concepts, such as aeroassisted orbital transfers and aerobraking, have been designed to mitigate the high heating rates such that the TPS weight can be minimized. Among those concepts, the use of a flow augmented thermal management system for entry and re-entry environments has shown some promises in reducing heat and drag loads. This concept relies on jet penetration from supersonic and hypersonic counterflow jets, that could significantly weaken and disperse the shock-wave system of the spacecraft flowfield to reduce wave drag and aerothermal loads. Greatly reducing wave drag and aerothermal loads significantly enhances aerothermal performance, allowing thinner or much lighter TPS to be used, which translates into spacecraft weight and cost savings. Other benefits include better aerodynamic efficiency and improved down-range and cross-range maneuverability. There are two jet penetration modes involved in a supersonic/hypersonic flow interacting with counterflow jets: short penetration mode (SPM) and long penetration mode (LPM) interactions. Previous studies have shown that the LPM jet significantly increases the shock stand-off distance, thus reducing the strength of bow shock, which leads to a reduction in wave drag. The LPM jet acts as, in essence, a "pencil" of fluid with high dynamic pressure, penetrating into the incoming freestream, to attenuate the shock system. Though the function of the LPM jet has been demonstrated in the previous study, further experimental and computational analyses through trade studies are required to determine the optimum operating conditions of the LPM jet.

The objective of this study is to provide a practical design approach to the development of flow control technologies as spacecraft subsystem(s) for better thermal management, aerodynamic efficiency, control authority and range, and improvements in payload mass fraction of the spacecraft in entry and re-entry atmospheres using counterflowing LPM jets to significantly modify/reshape the external flow environment and weaken the shock. To achieve this goal, we have conducted numerous time-accurate and steady-state computational fluid dynamics (CFD) simulations of the supersonic flow around an Apollo-type capsule with and without the counterflow jet using a Reynold-averaged Navier-Stokes (RANS) flow solver-- UNIC code. Axisymmetric RANS simulations were first conducted to investigate the grid convergence for this type of flowfield. Parametric studies of different freestream Mach numbers (3.48 and 4.96),

* Assistant Professor, Mechanical Engineering Dept., UAB, E-mail: gcheng@uab.edu
† Graduate research assistant, Mechanical Engineering Dept., UAB, E-mail: kdn@uab.edu
‡ President, Engineering Sciences, Inc., E-mail: ychen_esi@yahoo.com
§ Senior scientist, ER43, NASA MSFC, E-mail: ten-see.wang@nasa.gov
** Senior scientist, NASA MSFC

angles of attack (0^o and 10^o), and different counterflow jet mass flow rates and nozzle configurations using 3-D steady-state RANS simulations were performed to examine their effect of the drag and heat loads, and to explore the counterflow jet condition where LPM can be obtained. Some of the numerical results are plotted as shown in Figures 1-2. Numerical results and their comparisons with the test data will be detailed in the full-length paper.

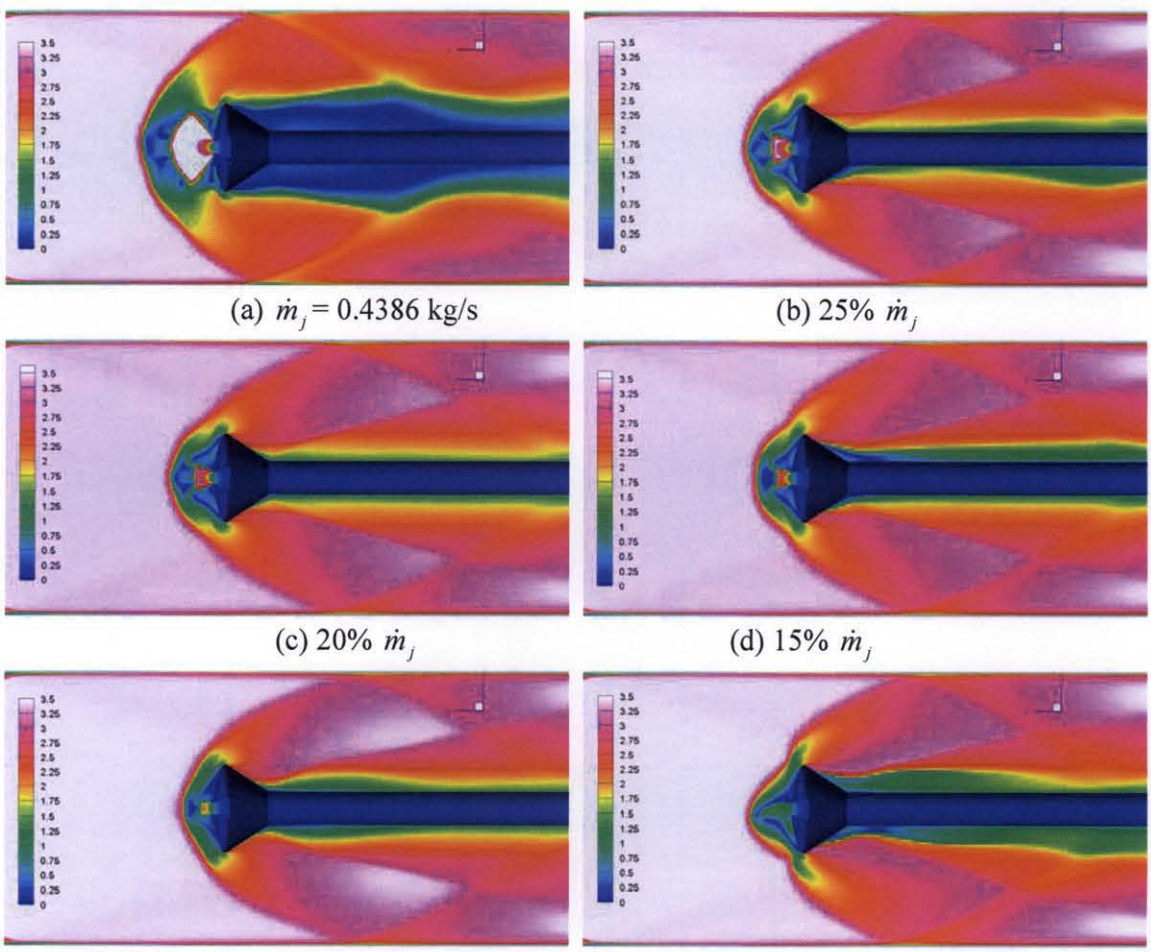

(a) $\dot{m}_j$ = 0.4386 kg/s (b) 25% $\dot{m}_j$

(c) 20% $\dot{m}_j$ (d) 15% $\dot{m}_j$

(e) 10% $\dot{m}_j$ (f) 5% $\dot{m}_j$

Figure 1: Mach number contours at the symmetry plane and the surfaces of the capsule and sting for different counter-flow jet mass flow rates (Mach no. = 3.48, Angle of attack = 0, counter-flow jet exit Mach number of 1)

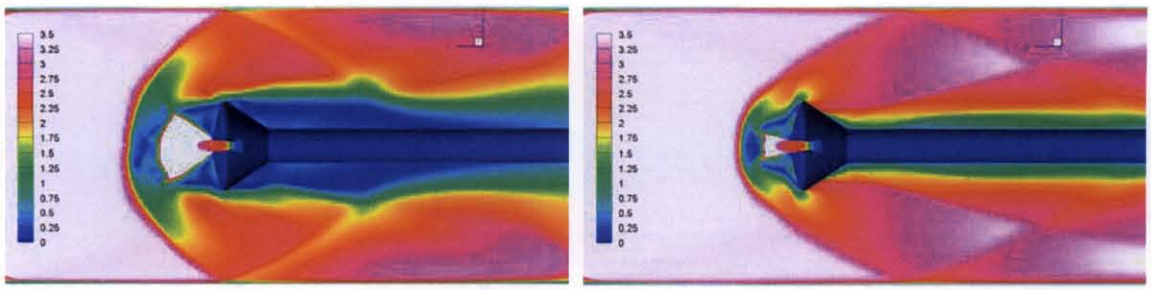

(a) $\dot{m}_j$ = 0.4386 kg/s

(b) 25% $\dot{m}_j$

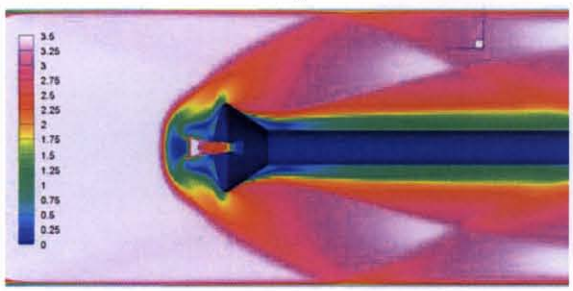

(c) 20% $\dot{m}_j$

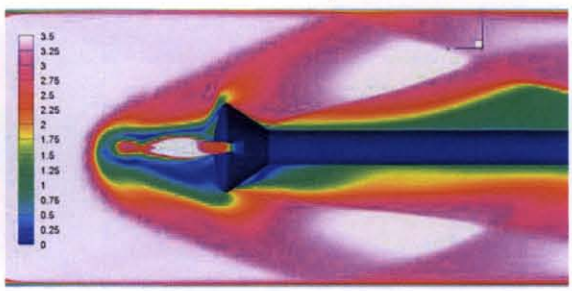

(d) 15% $\dot{m}_j$

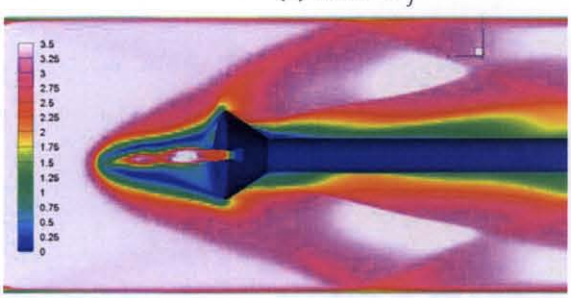

(e) 10% $\dot{m}_j$

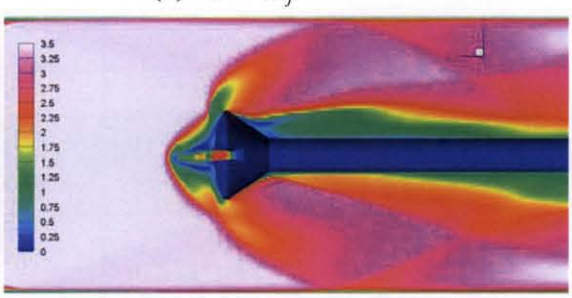

(f) 5% $\dot{m}_j$

Figure 2: Mach number contours at the symmetry plane and the surfaces of the capsule and sting for different counter-flow jet mass flow rates (Mach no. = 3.48, Angle of attack = 0, counter-flow jet exit Mach number of 2.44)

MSFC-199

Numerical Study of Flow Augmented Thermal Management for Entry and Re-entry Environments

Gary C. Cheng*, Kshitij D. Neroorkar†
Department of Mechanical Engineering
University of Alabama at Birmingham, Birmingham, AL 35294-4461

Yen-Sen Chen‡
Engineering Sciences, Inc., Huntsville, Alabama, 35815

and

Ten-See Wang§, Endwell O. Daso**
NASA Marshall Space Flight Center, Huntsville, Alabama, 35812

The use of a flow augmented thermal management system for entry and re-entry environments is one method for reducing heat and drag loads. This concept relies on jet penetration from supersonic and hypersonic counterflowing jets that could significantly weaken and disperse the shock-wave system of the spacecraft flowfield. The objective of this research effort is to conduct parametric studies of the supersonic flow over a 2.6% scale model of the Apollo capsule, with and without the counterflowing jet, using time-accurate and steady-state computational fluid dynamics simulations. The numerical studies, including different freestream Mach numbers, angles of attack, counterflowing jet mass flow rates, and nozzle configurations, were performed to examine their effect on the drag and heat loads and to explore the counterflowing jet condition. The numerical results were compared with the test data obtained from transonic blow-down wind-tunnel experiments conducted independently at NASA MSFC.

I. Introduction

NASA is currently looking to develop a crew launch vehicle (CLV). One of the challenges posed in designing this vehicle is to determine thermal protection system (TPS) requirements such that the structure integrity can be maintained during entry and re-entry into planetary and earth atmospheres, where tremendous amounts of heat and drag loads occur. Though various TPS's have been employed to manage the heat loads, the use of a TPS can substantially increase the weight of the vehicle. Hence, various concepts, such as aeroassisted orbital transfers and aerobraking, have been designed to mitigate the high heating rates so that the TPS weight can be minimized. Among those concepts, the use of a flow augmented thermal management system[1-4] for entry and re-entry environments has shown promise in reducing heat and drag loads. This concept relies on jet penetration from supersonic and hypersonic counterflowing jets that could significantly weaken and disperse the shock-wave system of the spacecraft flowfield to reduce wave drag and aerothermal loads, which enhances aerothermal performance, allowing a thinner or much lighter TPS to be used and translating into spacecraft weight and cost savings. Other benefits include better aerodynamic efficiency and improved down-range and cross-range maneuverability. There are two jet penetration modes involved in a supersonic/hypersonic flow interacting with counterflowing jets: short penetration mode (SPM) and long penetration mode (LPM) interactions. Previous studies[1, 5-6] have shown that the LPM jet significantly increases the shock stand-off distance, thus reducing the strength of bow shock, which could lead to a higher

* Associate Professor, Senior Member AIAA, E-mail: gcheng@uab.edu
† Graduate research assistant
‡ President, Member AIAA
§ Technical Assistant, ER43, Thermal and Combustion Analysis Branch, Senior Member AIAA
** AST, Aerospace Flight System, Senior Member AIAA

reduction in wave drag. The LPM jet acts as, in essence, a "pencil" of fluid with high dynamic pressure, penetrating into the incoming freestream to attenuate the shock system. Though the potential benefits of counterflowing jets has been demonstrated in the previous studies, further experimental and computational analyses are required to determine their optimum conditions.

It is extremely difficult and expensive to measure the detailed thermal-fluid environment around the vehicle under the actual flight conditions. Though some wind tunnel tests have been conducted to simulate the hypersonic flow environment during re-entry, these studies have been limited by the total pressure and enthalpy that the wind tunnel can operate. The objectives of this effort are 1) to conduct computational fluid dynamics (CFD) simulations to study the interaction between the bow shock and the counterflowing jet and its effects on the pressure and heat loads on the surface and 2) to validate and verify the numerical accuracy of the employed CFD code such that the code can be applied to simulate a wide range of actual flight conditions. An Apollo-type capsule, as shown in Figure 1, was used in the present study. Two different freestream Mach numbers (M_∞ = 3.48, and 4.96) at two different angles of attack (0° and 10°), along with different nozzles (nozzle exit M_j = 1, 2.44, and 2.94) and mass flow rates (1, 0.25, 0.2, 0.15, 0.1, and 0.05 lb/s) of the counterflowing jet, were investigated both numerically and experimentally. Numerical studies were actually conducted before experimental tests so that validation and verification of the CFD code could be neutral and meaningful. The computational methodology was based on an existing Unstructured-grid Navier-Stokes Internal-external computational fluid dynamics Code (UNIC[7-9]). The UNIC code has been well validated and employed to simulate a great variety of engineering problems ranging from internal to external flows, incompressible to compressible flows, single-phase to multi-phase flows, and inert to reacting flows. The result of experimental tests was reported earlier[1]. The numerical results and comparisons with the test data are reported herein.

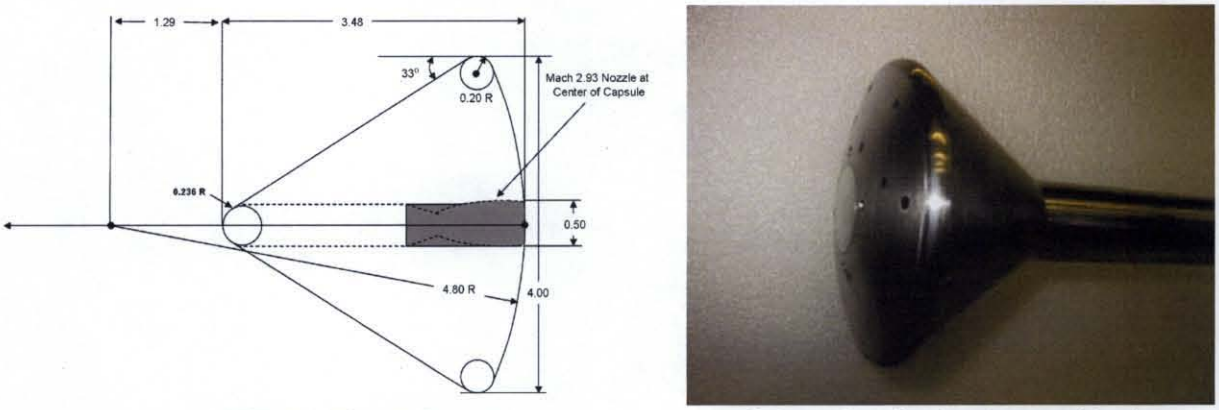

(a) Sketch of capsule **(b) Actual testing hardware with sting**

Figure 1. Subscale (2.6%) of Apollo capsule used in the wind tunnel test (dimension in inch).

II. Numerical Methodology

The employed CFD solver, UNIC, solves a set of Reynolds-averaged governing equations (continuity, Navier-Stokes, energy, species mass fraction, etc.) to satisfy the conservation laws for a turbulent flow of interest. The set of governing equation can be written in Cartesian tensor form:

$$\frac{\partial \rho}{\partial t} + \frac{\partial}{\partial x_j}(\rho V_j) = 0 \tag{1}$$

$$\frac{\partial (\rho V_i)}{\partial t} + \frac{\partial}{\partial x_j}(\rho V_j V_i) = -\frac{\partial p}{\partial x_i} + \frac{\partial \tau_{ji}}{\partial x_j} + S_V \tag{2}$$

$$\frac{\partial (\rho h_t)}{\partial t} + \frac{\partial}{\partial x_j}(\rho V_j h_t) = \frac{\partial p}{\partial t} + \frac{\partial}{\partial x_j}\left[\left(\frac{\mu}{\mathrm{Pr}} + \frac{\mu_t}{\mathrm{Pr}_t}\right)\frac{\partial h}{\partial x_j}\right] + \frac{\partial V_i \tau_{ji}}{\partial x_j} + Q_r + S_h \tag{3}$$

$$\frac{\partial (\rho k)}{\partial t} + \frac{\partial}{\partial x_j}(\rho V_j k) = \frac{\partial}{\partial x_j}\left[\left(\mu + \frac{\mu_t}{\sigma_k}\right)\frac{\partial k}{\partial x_j}\right] + \rho(P_k - \varepsilon) \tag{4}$$

$$\frac{\partial(\rho\varepsilon)}{\partial t}+\frac{\partial}{\partial x_j}(\rho V_j\varepsilon)=\frac{\partial}{\partial x_j}\left[\left(\mu+\frac{\mu_t}{\sigma_\varepsilon}\right)\frac{\partial\varepsilon}{\partial x_j}\right]+\rho\frac{\varepsilon}{k}\left(C_1P_k-C_2\varepsilon+C_3\frac{P_k^2}{\varepsilon}\right) \tag{5}$$

$$\frac{\partial(\rho\alpha_i)}{\partial t}+\frac{\partial}{\partial x_j}(\rho V_j\alpha_i)=\frac{\partial}{\partial x_j}\left[\left(\frac{\mu}{Sc}+\frac{\mu_t}{Sc_t}\right)\frac{\partial\alpha_i}{\partial x_j}\right]+S_i \tag{6}$$

$$\tau_{ji}=(\mu+\mu_t)\left(\frac{\partial V_i}{\partial x_j}+\frac{\partial V_j}{\partial x_i}-\frac{2}{3}\frac{\partial V_l}{\partial x_l}\delta_{ij}\right)-\frac{2}{3}\rho k\delta_{ij}\;;\quad P_k=\mu_t\left(\frac{\partial V_i}{\partial x_j}+\frac{\partial V_j}{\partial x_i}-\frac{2}{3}\frac{\partial V_l}{\partial x_l}\delta_{ij}\right)\frac{\partial V_i}{\partial x_j} \tag{7}$$

where ρ is the fluid density p is the pressure, V_j = (u, v, w) stands for the velocity components in x-, y-, and z-coordinates respectively, h_t and h are the total and static enthalpies, k is the turbulence kinetic energy, P_k and ε are the production and dissipation rates of turbulence, α_i and S_i are the mass fraction and production/destruction rate of i-th species, Q_r is the radiative heat flux, S_V and S_h are the source/sink terms of the momentum and energy equations, μ and μ_t are the fluid and eddy viscosity, τ_{ji} represents the sum of the viscous and Reynolds stresses, Pr and Pr$_t$ are the Prandtl and turbulent Prandtl numbers, Sc and Sc_t are Schmidt and turbulent Schmidt numbers, and C_1, C_2, C_3, σ_k, and σ_ε are turbulence modeling constants. Detailed expressions for the k-ε models and wall functions can be found in [10]. An extended k-ε turbulence model[11] was used to close the system of Reynolds-averaged governing equations. A modified wall function approach[12, 13] was employed to provide wall boundary layer solutions that are less sensitive to the near-wall grid spacing.

A predictor and multi-corrector pressure-based solution algorithm[14, 15] was employed in the UNIC code to couple the set of governing equations such that both compressible and incompressible flows can be solved in a unified framework without using ad-hoc artificial compressibility and/or a pre-conditioning method. The employed predictor-corrector solution method[5] is based on modified pressure-velocity coupling approach of the SIMPLE-type[15] algorithm, which includes the compressibility effects and is applicable to flows at all speeds. In order to handle problems with complex geometries, the UNIC code employs a cell-centered unstructured finite volume method[8, 9] to solve for the governing equations in the curvilinear coordinates, in which the primary variables are the Cartesian velocity components, pressure, total enthalpy, turbulence kinetic energy, turbulence dissipation and mass fractions of chemical species.

The inviscid flux is evaluated through the values at the upwind cell and a linear reconstruction procedure to achieve second order accuracy. A multi-dimensional linear reconstruction approach by Barth and Jespersen[16] is used in the cell reconstruction to achieve higher-order accuracy for the convection terms. A second-order central-difference scheme is employed to discretize the diffusion fluxes and source terms. A dual-time sub-iteration method is employed for time-accurate time-marching computations. A pressure damping term, Rhie and Chow[17], is applied to the evaluation of mass flux at the cell interface to avoid the even-odd decoupling of velocity and pressure fields. All the discretized governing equations are solved using the preconditioned Bi-CGSTAB[18] matrix solver, except the pressure-correction equation which has an option to be solved using GMRES[19] matrix solver when the matrix is ill-conditioned. An algebraic multi-grid (AMG) solver[20] is included that users can activate to improve the convergence, if desired. In order to efficiently simulate problems involving large numbers of meshes, the UNIC code employed parallel computing with domain decomposition, where the exchange of data between processors is done by using MPI[21]. Domain decomposition (partitioning the computational domain into several sub-domains handled by different computer processors) can be accomplished by using METIS[22] or a native partitioning routine in the UNIC code. In addition, several physical submodels were incorporated in the code to simulate problems involving multiple physics. Among them, two are related to the present study. The first one is a point implicit method[23], which was used to resolve stiffness problems associated with the source term of the species transport equation when combustion occurs. In this study, a finite-rate air chemistry model was employed to simulate air dissociation. However, it was later found that chemical reactions did not take place due to low temperatures for the entire flowfield (the low total enthalpy problem mentioned earlier). The second one is a conjugate heat transfer (CHT) formulation[24, 25] for coupling fluid dynamics and conductive heat transfer in solids. This capability will enable us to calculate the heat flux to the wall and wall temperatures without specifying wall surface temperatures, which sometimes are unknown. It should be noted that a wall temperature of 300 K was specified in this study, and thus the CHT model was not used. This may lead to some errors in calculating the heat flux to the face of the capsule.

III. Numerical Meshes

In the present study, Gridgen® was used to generate meshes describing the geometries of the nozzle of the counterflowing jet, the capsule, support sting, and the wind tunnel. A quadrilateral mesh system (for 2-D cases) and a hexahedral mesh system (for 3-D cases) were employed to avoid over-predicting jet spreading rate caused by large numerical diffusion associated with triangular mesh (in 2-D) and tetrahedral mesh (in 3-D). Two sample mesh systems are demonstrated in Figures 2-3. It can be seen that only half of the wind tunnel test section and the capsule were simulated by assuming symmetry at the mid-plane. A grid sensitivity study was conducted using 2-D numerical simulations for three different counterflowing jet nozzle configurations to optimize the grid spacing needed. There are three nozzle configurations simulated in this study, where Nozzles #1, #2, and #3 have counterflowing jet exit Mach numbers (M_j) of unity, 2.44 and 2.94, respectively. In addition, two angles of attack (α = 0° and 10°) were studied. The employed mesh systems for different nozzle configurations and angles of attack are listed in Table 1.

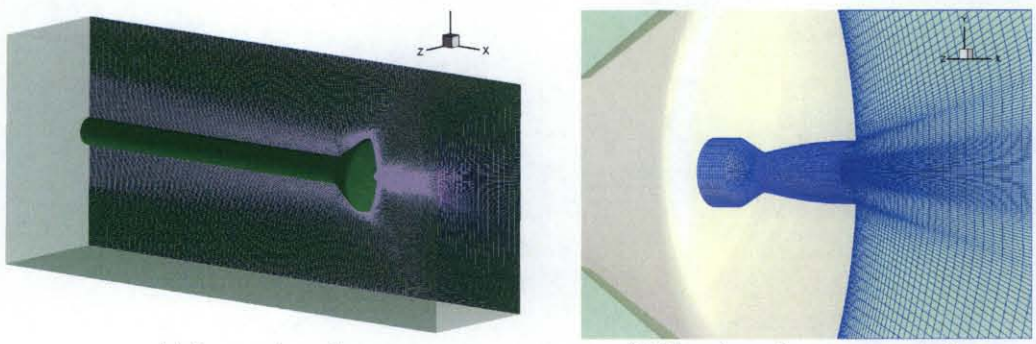

(a) Symmetry plane **(b) Nozzle and near capsule face**

Figure 2. Mesh system for the test cases of 0° angle of attack and M_j = 2.44.

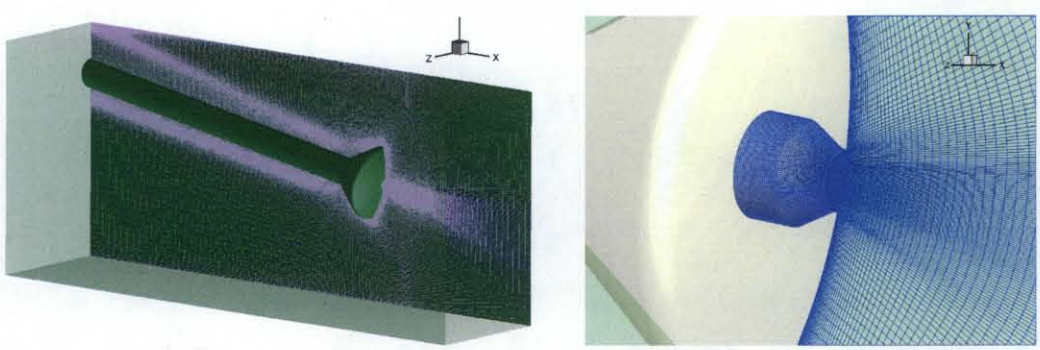

(a) Symmetry plane **(b) Nozzle and near capsule face**

Figure 3. Mesh system for the test cases of 10° angle of attack and M_j = 1.

	Angle of attack	No. of nodes	No. of cells
No nozzle	0°	930K	1.05M
	10°	980K	1.1M
Nozzle #1	0°	1.1M	1.4M
	10°	1.1M	1.4M
Nozzle #2	0°	1M	1.5M
	10°	950K	1.4M
Nozzle #3	0°	1M	1.5M
	10°	950K	1.4M

Table 1. Mesh systems for simulated configuration with different nozzles and angles of attack

IV. Results and Discussion

In total, 26 cases were simulated in this study. These include two freestream Mach numbers (M_∞ = 3.48 and 4.96) and two angles of attack (α = 0 and 10) for the capsule with and without the counterflowing jet. For the capsule with the counterflowing jet, three different nozzles, which in respect produce exit Mach numbers of M_j = 1,

2.44 and 2.94, with a mass flow rate of 1 lb/s were investigated at each freestream Mach number and angle of attack. Furthermore, five additional jet mass flow rates ($\dot{m}_j$ = 0.25, 0.2, 0.15, 0.1, and 0.05 lb/s) for two different nozzles (M_j = 1 and 2.44) were simulated to study the effect of jet flow rate on pressure, heat flux and shock penetration mode. All the nozzles of the counterflowing jet have an exit diameter of 0.5". The flow conditions of freestream and counterflowing jets simulated are summarized in Table 2. A series of axisymmetric simulations were conducted for the three counterflowing jet nozzle configurations using different grid resolutions (201x35, 301x51, and 351x61 for axial and radial directions) to obtain the actual chamber conditions for the 3-D simulations of the full configuration. These studies were designed to ensure that the Mach number at the exit of different counterflowing jet nozzles match the designed values. The actual chamber conditions are slightly different from the designed values based on the 1-D isentropic correlation. The numerical results of these test cases are organized into three sections for the ease of understanding. The first section is focused on the effect of jet mass flow rates on the penetration mode and the pressure as well as heat flux at the capsule face. Comparisons of numerical results of two different jet nozzles at the freestream Mach number of 3.48 and 0° angle of attack will be employed for the demonstration. The second section illustrates the effect of the freestream Mach number, where the angle of attack and jet flow rate remain the same. The last section will compare the result for different angles of attack at the same freestream and counterflowing jet conditions. Once again, it should be noted that numerical simulations were conducted before the experimental tests, and the comparisons shown here were done after the test data became available. The test data used in comparison and detailed information about the wind tunnel test have been described in Ref. 1. The locations of pressure and heat flux sensors at the capsule face are illustrated in Figure 5, where the blue circles mark the location of heat flux sensors, and the red crosses indicate the location of pressure sensors. In the following sections, Rows 1, 2 and 3 are designated to represent the locations at the radius of 1.625", 1.25" and 0.875", respectively.

Free stream conditions					Nozzle conditions					
M_∞	P_0 (atm)	P (atm)	T_0 (K)	T (K)	M_j	$\dot{m}$ (lb/s)	P_0 (atm)	P (atm)	T_0 (K)	T (K)
3.48	3.061	0.04129	333.33	97.406	0	0	---	---	---	---
					1	1	15.6889	15.2949	300	297.83
						0.25	3.9223	3.8238	300	297.83
						0.2	3.1378	3.0590	300	297.83
						0.15	2.3534	2.2943	300	297.83
						0.1	1.5689	1.5295	300	297.83
						0.05	0.7845	0.7648	300	297.83
					2.44	1	37.9252	36.9126	300	297.69
						0.25	9.4813	9.2282	300	297.69
						0.2	7.5850	7.3825	300	297.69
						0.15	5.6888	5.5369	300	297.69
						0.1	3.7925	3.6913	300	297.69
						0.05	1.8963	1.8456	300	297.69
					2.94	1	60.6803	59.0521	300	297.68
4.96	5.442	0.01078	333.33	56.303	0	0	---	---	---	---
					1	1	15.6889	15.2949	300	297.83
					2.44	1	37.9252	36.9126	300	297.69
					2.94	1	60.6803	59.0521	300	297.68

Table 2. Boundary conditions for the freestream and counterflowing jet.

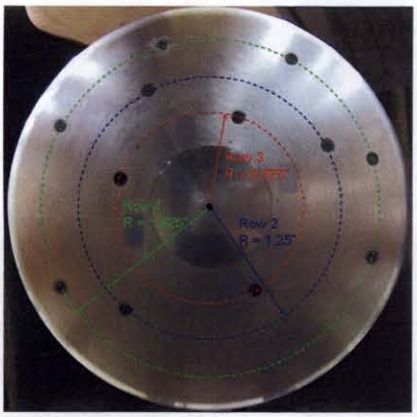

(a) Front view of the test article

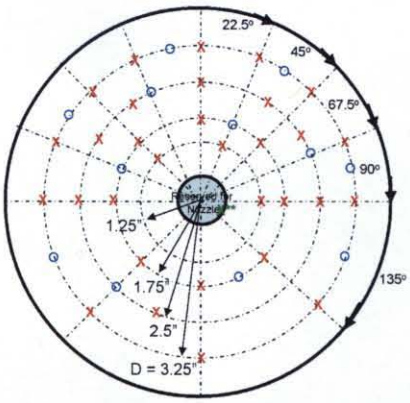

(b) Layout of pressure and heat flux sensors

Figure 4. Locations of pressure and heat flux sensors at the face of the capsule.

A. Effect of counterflowing jet:

The effect of different mass flow rates of the counterflowing jet on the pressure and heat loads on the capsule face is examined as follows. As shown in Table 2, the effect of counterflowing jet mass flow rates on the pressure and temperature at the capsule face as well as shock-jet interaction were simulated for the freestream Mach number of 3.48 and jet exit Mach numbers of 0 (no jet), 1, and 2.44. The result of the case without a counterflowing jet is used as the baseline to demonstrate the change of pressure and heat flux at the capsule face due to different jet flow rates and Mach numbers. The predicted flowfield of the baseline case is plotted in Figure 5, which shows the contours of pressure, temperature and Mach number at the symmetry plane and the surface of the capsule as well as the support sting. All shock structures are well captured by the numerical simulation. In Figure 6, the contour plot of the pressure gradient from the numerical simulation is compared to the Schlieren image from the wind tunnel test, which shows agreement on the shock stand-off distance. The predicted heat flux and pressure distributions on the capsule face in the angular direction (at 3 different radii-- 1.625", 1.25", and 0.875") are plotted in Figure 7. The experimental test reported that the heat fluxes are 13033±38%, 15308±7%, and 13277±9% W/m^2 at Rows 1, 2, and 3, respectively. The pressures at Rows 1, 2, and 3 were measured to be 8.66, 8.58, and 8.5 atm, respectively. It is obvious that the heat flux is over-predicted, while the pressure is under-predicted. Smaller pressure predicted at the capsule face indicates higher kinetic energy of the flow near the face, which attributes to higher heat flux to the wall when compared with the test data. The cause for the discrepancy will be discussed later along with the results for those cases with the counterflowing jet. In Figure 7, a time history of the drag force acting on the capsule face is also illustrated, which shows the flow is very steady except at the beginning of the numerical calculation.

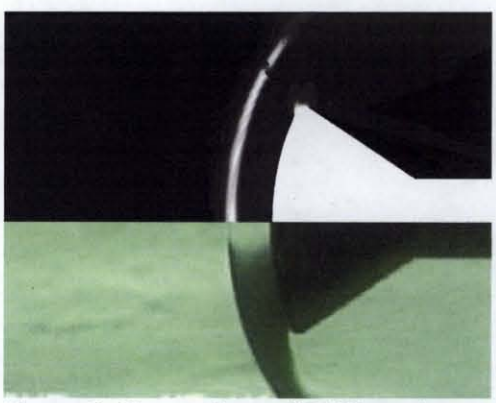

Figure 6. Comparisons of Schlieren image from experiments (bottom) and pressure gradients from numerical simulations (top) for $M_\infty = 3.48$ and $M_j = 0$.

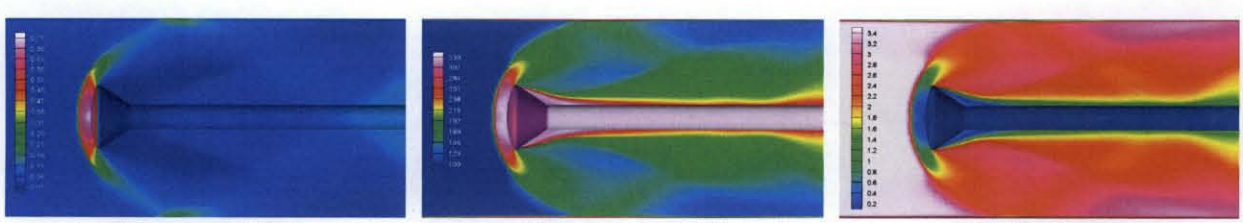

(a) pressure (atm) (b) temperature (K) (c) Mach no.

Figure 5. Pressure, temperature and Mach no. contours at the symmetry plane and surfaces of capsule and support sting for $M_\infty = 3.48$ and $M_j = 0$.

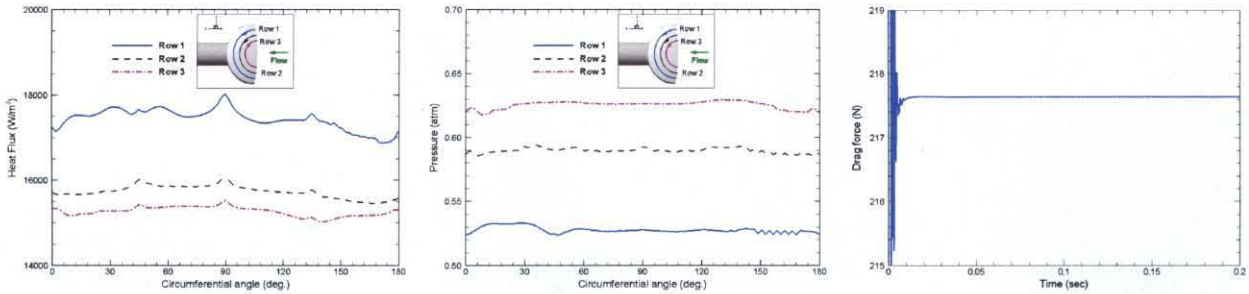

(a) heat flux distribution (b) pressure distribution (c) time history of drag force

Figure 7. Comparisons of Schlieren image from experimental tests (bottom) and pressure gradients from numerical simulations (top) for $M_\infty = 3.48$ and $M_j = 0$.

Two different nozzles were used to eject the counterflowing jet, and six different jet flow rates were analyzed for each nozzle. Figures 8-9 demonstrate comparisons of pressure and temperature distributions for the counterflowing jet exit Mach number of 1 with various jet flow rates. It can be clearly seen that for the counterflowing jet exit Mach number of 1, a long penetration mode (LPM) occurs at the jet mass flow rate of 0.05 lb/s. In addition, the counterflowing jet becomes unstable for the case of 0.05 lb/s jet flow rate. However, in the experimental test, LPM occurs at the jet flow rates of 0.1 and 0.05 lb/s. This discrepancy is confirmed by the comparison of the predicted pressure gradient contours with the Schlieren picture, shown in Figure 10, which indicates that the predicted shock stand-off distance agrees very well with the test data for the case of 0.05 lb/s jet flow rate, but which fails to match the test data for the jet flow rate of 0.1 lb/s. In Figures 11 and 12, the calculated pressure and heat flux distributions on the capsule face at three different radial locations are compared to those of the baseline case to show the effect of different jet mass flow rates. The comparison of numerical results indicates that both the heat flux and pressure at the capsule face decrease as the mass flow rate of the counterflowing jet increases, except for the case with a jet flow rate of 0.05 lb/s.

For the counterflowing jet at an exit Mach number of 2.44, pressure and temperature distributions for various jet flow rates are compared in Figures 13-14. It can be clearly seen that LPM occurs in the cases with the jet flow rates of 0.15, 0.1 and 0.05 lb/s. All three cases with LPM show unsteadiness of the jet-shock structure, and the case of 0.05 lb/s jet flow rate is the most unstable one. The comparison of the predicted pressure gradient contour with the Schlieren image shown in Figure 15 confirms the occurrence of LPM for the jet flow rates of 0.1 and 0.05 lb/s (no test data available for 0.15 lb/s jet flow rate). More importantly, the predicted shock stand-off distance agrees with the test data very well. The calculated pressure and heat flux distributions on the capsule face show the similar trend as those of the exit Mach number of 1, and hence will not be plotted here again.

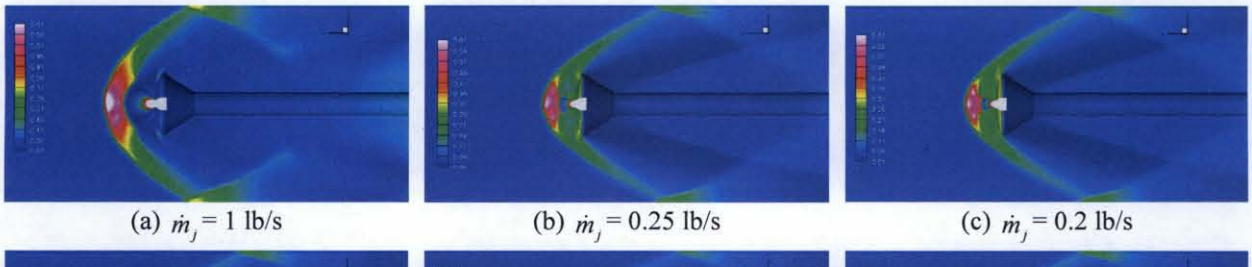

(a) $\dot{m}_j = 1$ lb/s (b) $\dot{m}_j = 0.25$ lb/s (c) $\dot{m}_j = 0.2$ lb/s

(d) $\dot{m}_j = 0.15$ lb/s (e) $\dot{m}_j = 0.1$ lb/s (f) $\dot{m}_j = 0.05$ lb/s

Figure 8. Pressure contours (in atm) at the symmetry plane with different mass flow rates of counterflowing jet ($M_\infty = 3.48$, $M_j = 1$).

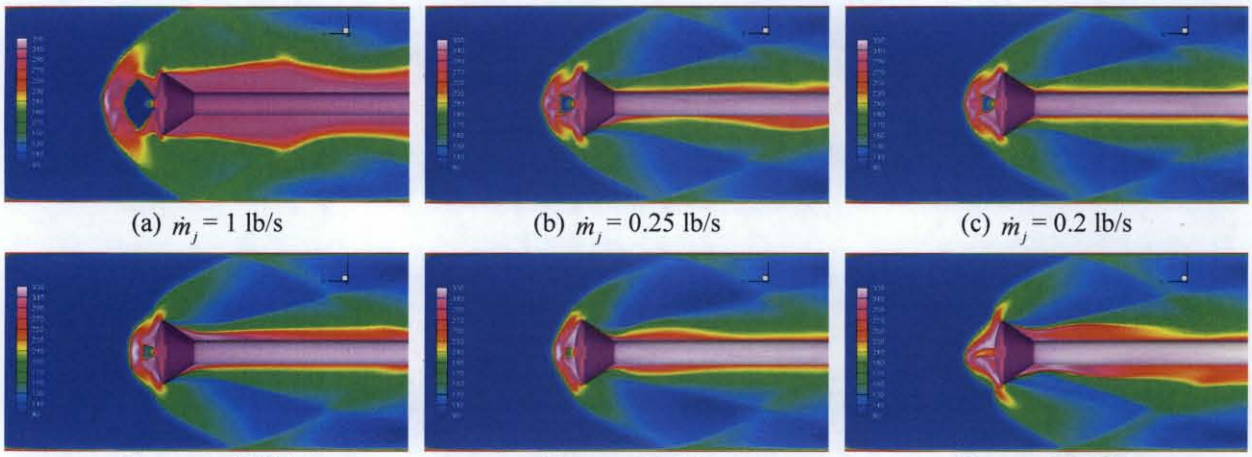

(a) $\dot{m}_j = 1$ lb/s (b) $\dot{m}_j = 0.25$ lb/s (c) $\dot{m}_j = 0.2$ lb/s

(d) $\dot{m}_j = 0.15$ lb/s (e) $\dot{m}_j = 0.1$ lb/s (f) $\dot{m}_j = 0.05$ lb/s

Figure 9. Temperature contours (in K) at the symmetry plane with different mass flow rates of counterflowing jet ($M_\infty = 3.48$, $M_j = 1$).

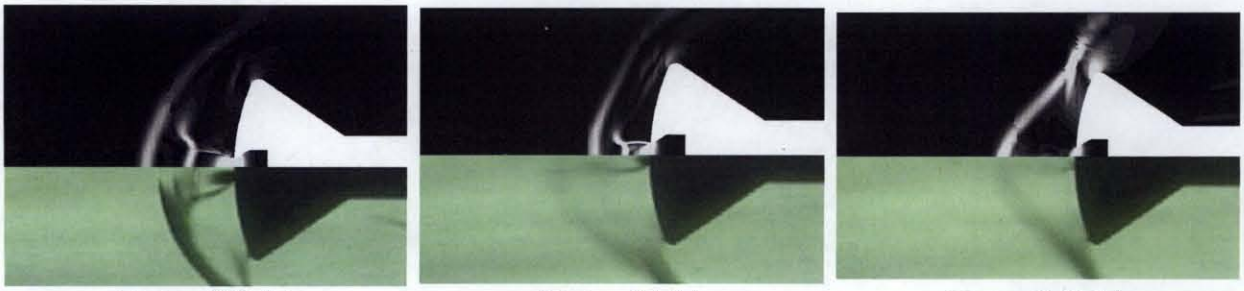

(a) $\dot{m}_j = 0.25$ lb/s (b) $\dot{m}_j = 0.1$ lb/s (c) $\dot{m}_j = 0.05$ lb/s

Figure 10. Comparisons of Schlieren image from experimental tests (bottom) and pressure gradients from numerical simulations (top) for $M_\infty = 3.48$ and $M_j = 1$.

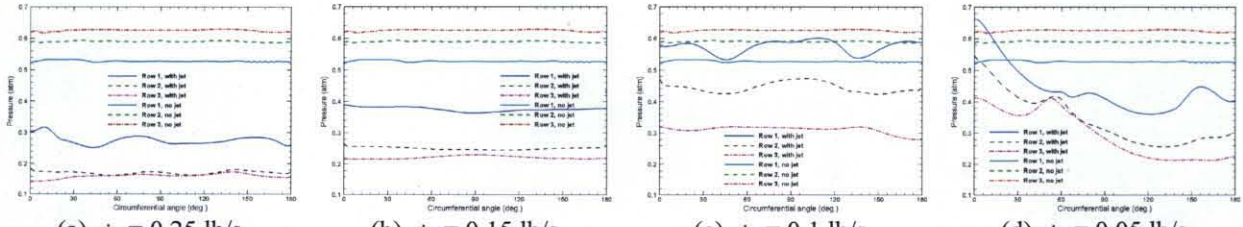

(a) $\dot{m}_j = 0.25$ lb/s (b) $\dot{m}_j = 0.15$ lb/s (c) $\dot{m}_j = 0.1$ lb/s (d) $\dot{m}_j = 0.05$ lb/s

Figure 11. Pressure distributions at capsule face with different mass flow rates of counterflowing jet ($M_\infty = 3.48$, $M_j = 1$).

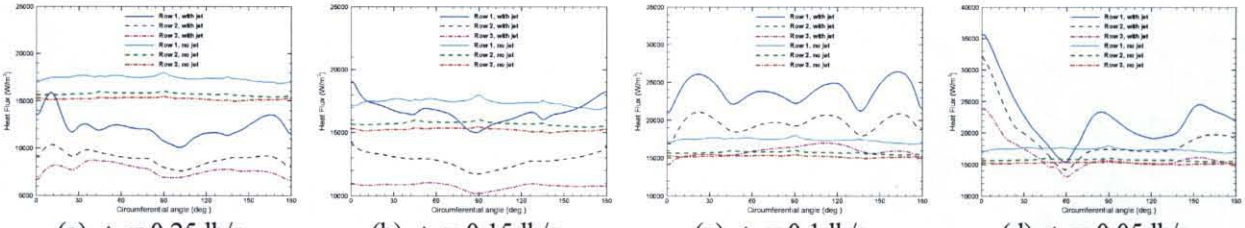

(a) $\dot{m}_j = 0.25$ lb/s (b) $\dot{m}_j = 0.15$ lb/s (c) $\dot{m}_j = 0.1$ lb/s (d) $\dot{m}_j = 0.05$ lb/s

Figure 12. Heat flux distributions at capsule face with different mass flow rates of counterflowing jet ($M_\infty = 3.48$, $M_j = 1$).

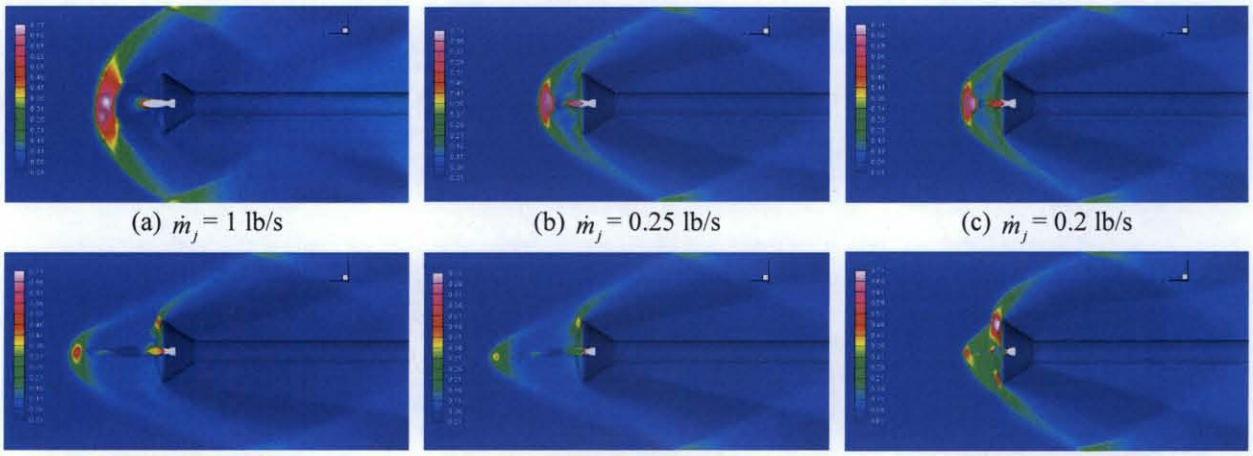

(a) $\dot{m}_j$ = 1 lb/s (b) $\dot{m}_j$ = 0.25 lb/s (c) $\dot{m}_j$ = 0.2 lb/s

(d) $\dot{m}_j$ = 0.15 lb/s (e) $\dot{m}_j$ = 0.1 lb/s (f) $\dot{m}_j$ = 0.05 lb/s

Figure 13. Pressure contours (in atm) at the symmetry plane with different mass flow rates of counterflowing jet (M_∞ = 3.48, M_j = 2.44).

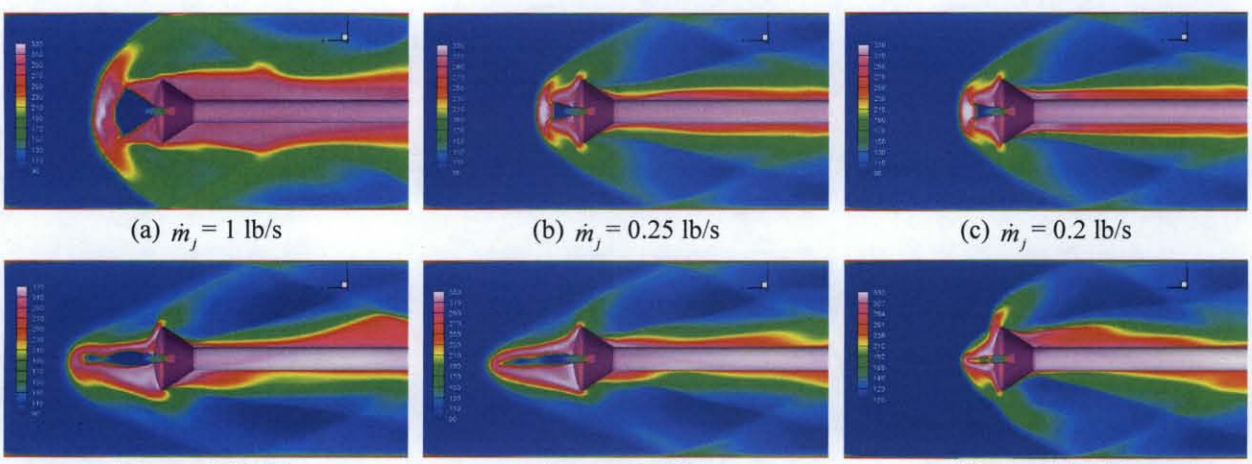

(a) $\dot{m}_j$ = 1 lb/s (b) $\dot{m}_j$ = 0.25 lb/s (c) $\dot{m}_j$ = 0.2 lb/s

(d) $\dot{m}_j$ = 0.15 lb/s (e) $\dot{m}_j$ = 0.1 lb/s (f) $\dot{m}_j$ = 0.05 lb/s

Figure 14. Temperature contours (in K) at the symmetry plane with different mass flow rates of counterflowing jet (M_∞ = 3.48, M_j = 2.44).

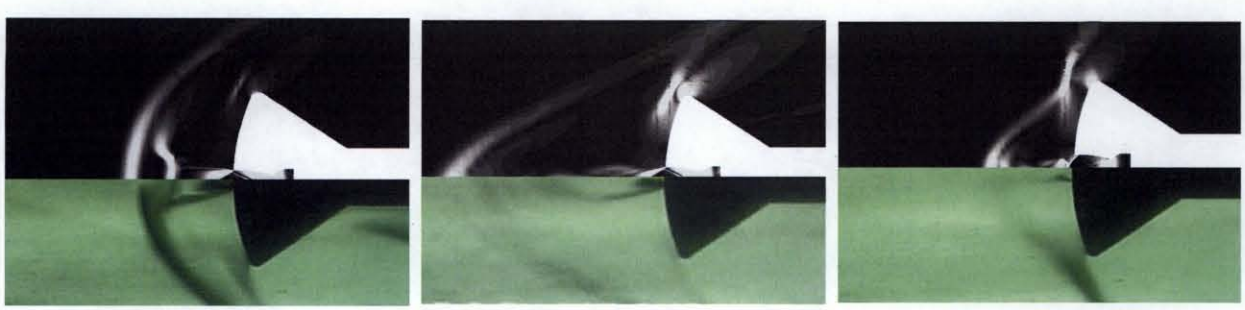

(a) $\dot{m}_j$ = 0.25 lb/s (b) $\dot{m}_j$ = 0.1 lb/s (c) $\dot{m}_j$ = 0.05 lb/s

Figure 15. Comparisons of Schlieren image from experimental tests (bottom) and pressure gradients from numerical simulations (top) for M_∞ = 3.48 and M_j = 2.44.

To summarize the effect of counterflowing jet flow rates, the predicted pressure and heat flux on the capsule face are compared to the test data and are plotted in Figures 16-17. As can be seen in Figures 11-12, pressure and

heat flux distributions at a given radial location are non-uniform. Hence, the line or symbol along with its error bar plotted in Figures 16-17 represent the mean value and its range of deviation at each radial locations for a given jet flow rate. In comparison of the heat flux at the capsule face, the numerical result has a similar trend to the test data, but over-predicts the magnitude of the heat flux. The difference is even larger at higher counterflowing jet flow rates, where the test data reveal negative heat flux (i.e. surface temperature is higher than the temperature of the flow near the wall). This could be caused by the numerical error of the employed flow solver. However, it should be noted that the magnitude of heat flux is very low because the temperature of the flow near the capsule face is very close to the stagnation temperature (300 K) of the counterflowing jet, as can be seen in Figures 9 and 14. Hence, the magnitude of heat flux is very sensitive to the surface temperature (300 K) specified in the numerical simulation. As mentioned earlier in the numerical methodology section, the use of a conjugate heat transfer model, where a fixed temperature is specified in the virgin layer of the material, should provide a more accurate calculation of the heat flux because its temperature is much less influenced by the heat exchange between the fluid flow and the solid material. Nevertheless, most importantly this preliminary study predicts a correct qualitative trend: the heat flux is reduced as the counterflowing jet flow rate increases, except those cases (0.05 lb/s jet flow rate for $M_j = 1$ and 0.05, 0.1 and 0.15 lb/s jet flow rate for $M_j = 2.44$) where LPM occurs. For the surface pressure comparison, Figure 17 reveals two major discrepancies between the numerical result and test data. The first major discrepancy is that the test data indicate the pressure is almost constant regardless of the jet flow rate, whereas the numerical results show pressure decreases as the jet flow rate increases except for those cases where LPM occurs. The test data somehow contradict another observation[2, 4] of drag reduction by the counterflowing jet, whereas this phenomenon is predicted by the numerical simulation and will be summarized in the following section. The second major discrepancy is that the predicted pressure levels are consistently lower than those observed in the measured data. Once of the possibilities which cause the discrepancy is the over-prediction of the spreading rate of the counterflowing jet, which leads to a smaller but stronger recirculation zone near the capsule face. It is a well known problem that the two-equation turbulence models tend to over-predict the jet spreading rate due to the compressibility effect[26-28]. A smaller but stronger recirculation zone near the capsule face will have a larger dynamic pressure and thus lower static pressure. This phenomenon can be observed by drawing an analogy of comparing the recirculating flow structure of larger jet expansion ($\dot{m}_j = 0.25$ lb/s) to that of smaller jet expansion ($\dot{m}_j = 0.1$ lb/s), as shown in Figure 18, where the larger jet expansion has smaller but stronger recirculation and thus lower pressure. In spite of these observations, further study is needed to assess the accuracy of numerical solutions and uncertainty of the test data.

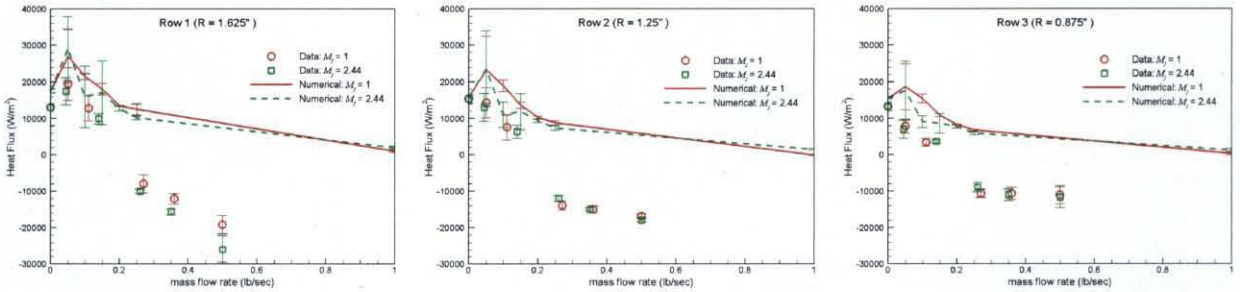

Figure 16. Comparisons of heat flux to capsule face at different radial locations with different Mach numbers and flow rates of counterflowing jet ($M_\infty = 3.48$).

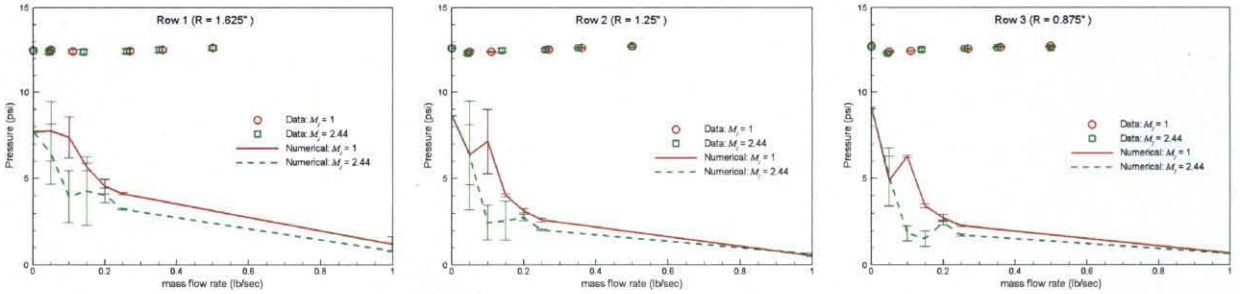

Figure 17. Comparisons of pressure on capsule face at different radial locations with different Mach numbers and flow rates of counterflowing jet ($M_\infty = 3.48$).

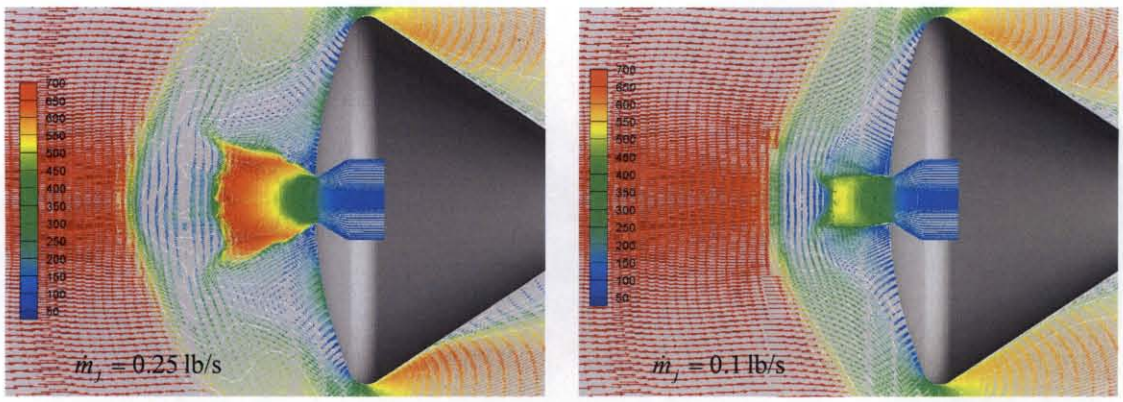

Figure 18. Velocity vectors (colored with magnitude) near capsule face (M_∞ = 3.48, M_j = 1).

In addition to the effect of jet flow rate, the effect of jet Mach number was also examined. Figure 19 shows the comparison of pressure and heat flux distributions along three angular planes between different jet Mach numbers with the same jet flow rate. Several features can be observed from the comparison: 1) All three cases with different jet Mach numbers do not exhibit circumferential uniformity; 2) A higher jet Mach number has a larger pressure reduction, but the effect of the jet Mach number on the heat flux is minimal and is within the range of uncertainty; and 3) Both pressure and heat flux show asymmetric phenomena, which indicate possible flow unsteadiness. The last feature is confirmed by the time history of the drag force and heat flux on the capsule face, as shown in Figures 20-21. However, unlike the case with low jet flow rates, the magnitude of unsteadiness is very small, which can be seen from the pressure and temperature contour plots shown earlier.

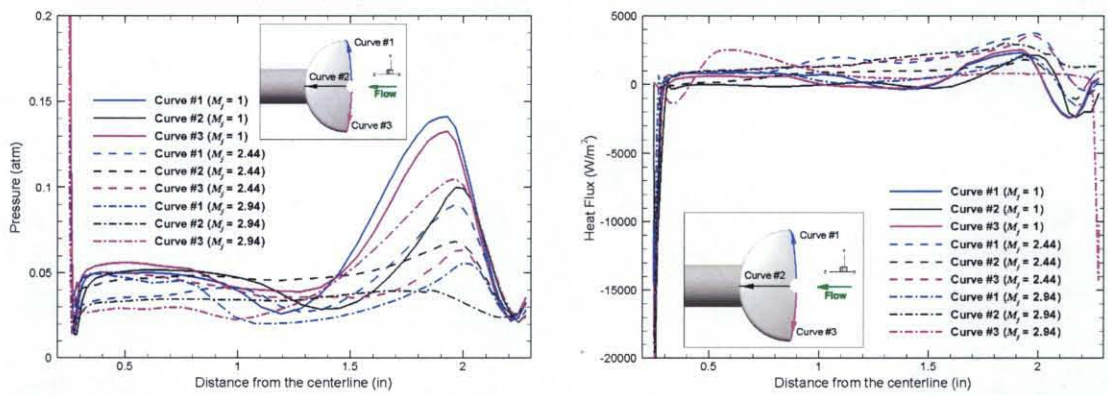

Figure 19. Pressure and heat flux distributions at 3 angular locations for different jet Mach no. (M_∞ = 3.48, α = 0, $\dot{m}_j$ = 1 lb/s).

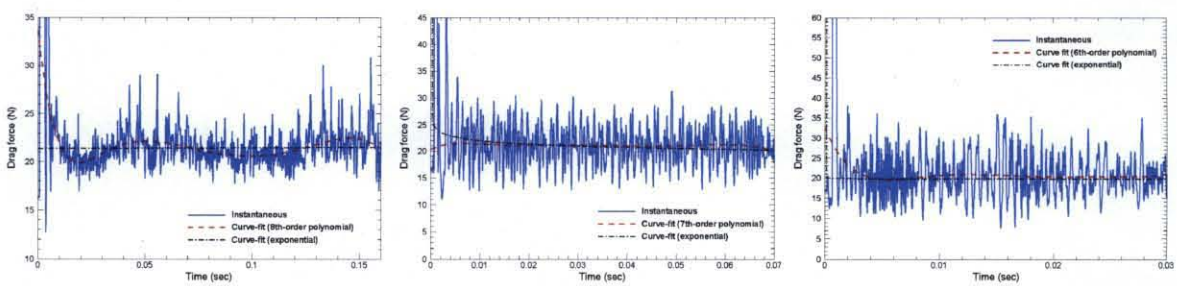

(a) M_j = 1 (b) M_j = 2.44 (c) M_j = 2.94

Figure 20. Time history of drag force on capsule face (M_∞ = 3.48, α = 0, $\dot{m}_j$ = 1 lb/s).

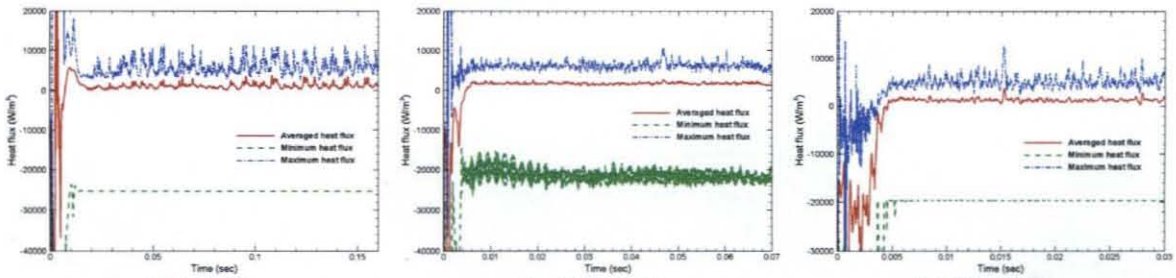

(a) $M_j = 1$ (b) $M_j = 2.44$ (c) $M_j = 2.94$

Figure 21. Time history of the min., max., and mean heat flux to the capsule face ($M_\infty = 3.48$, $\alpha = 0$, $\dot{m}_j = 1$ lb/s)

B. Freestream Mach number of 4.96:

In addition the freestream Mach number of 3.48, a set of simulations with a freestream Mach number of 4.96 were also conducted to study the reduction of pressure and heat loads by the counterflowing jet at different freestream conditions. Only mass flow rate of the counterflowing jet (1 lb/s) was simulated for this freestream Mach number. The calculated flowfields for different jet Mach numbers are plotted in Figure 21. The comparison of the pressure at the capsule face between two different freestream Mach numbers with the same jet Mach number is shown in Figure 23 while the comparison of the heat flux is illustrated in Figure 24. It can be seen that the difference is significant when there is no counterflowing jet due to different freestream conditions. However, the difference is small when the counterflowing jet is applied because the flow properties near the capsule face are dominated by the jet flow and are less influenced by the freestream conditions. This phenomenon demonstrates one of the advantages of using the counterflowing jet, the flow properties near the capsule face remain fairly constant throughout a wide range of flight conditions. However, a wider range of flight conditions need to be examined to attest this observation. The numerical results are summarized later to compare with all other cases simulated in this study.

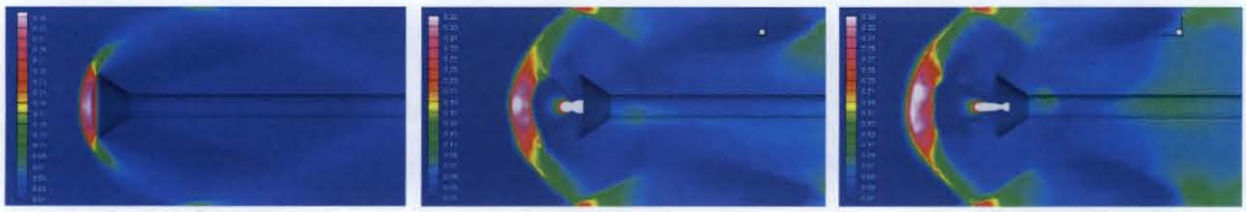

(a) No jet (b) $M_j = 1$ (c) $M_j = 2.44$

Figure 22. Pressure contours at the symmetry plane and surfaces of capsule and support sting ($M_\infty = 4.96$, $\alpha = 0$, $\dot{m}_j = 1$ lb/s).

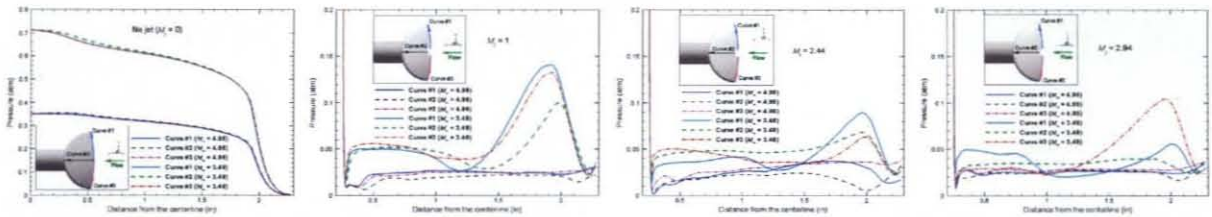

Figure 23. Comparisons of pressure distributions at capsule face with different freestream and jet Mach no.

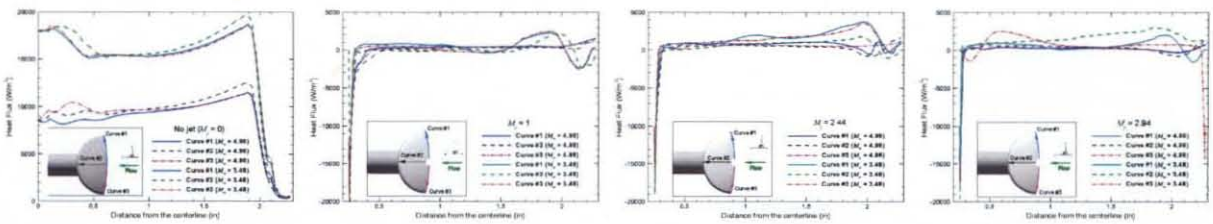

Figure 24. Comparisons of heat flux distributions at capsule face with different freestream and jet Mach no.

C. 10-degree angles of attack:

Other than the angle of attack of 0°, different freestream Mach numbers and jet Mach numbers with an angle of attack of 10° were simulated to study the impact of the counterflowing jet at different angles of attack. The counterflowing jet has a mass flow rate of 1 lb/s for all the cases with a 10° angle of attack. Some of the numerical results are plotted as shown in Figure 26. To demonstrate the effect of a counterflowing jet at this angle of attack, heat flux and pressure distributions at the capsule face were compared for different jet Mach numbers, as shown in Figures 27 and 28. It can be seen that the counterflowing jet has greatly reduced both the pressure and heat loads. In addition, the pressure and heat loads for 0° and 10° angles of attack are compared in Figures 29 and 30, which show that at the windward side (Curve #1) the pressure and heat flux are much higher when an angle of attack presents. Similar to the results obtained for cases with no angle of attack, the results for different counterflowing jet nozzles are very similar, which implies that this effect is weak. The drag, lift and heat flux, calculated by the CFD model, for different freestream and counterflowing jet conditions are summarized in Table 3.

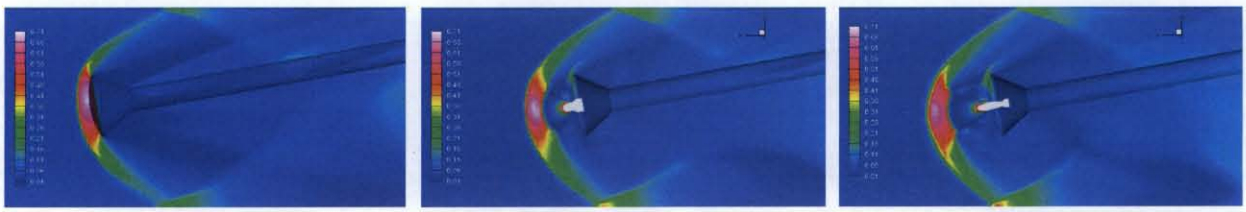

(a) No jet, $\dot{m}_j = 0$ lb/s (b) $M_j = 1$, $\dot{m}_j = 1$ lb/s (c) $M_j = 2.44$, $\dot{m}_j = 1$ lb/s

Figure 26. Pressure contours at the symmetry plane and surfaces of capsule and support sting ($M_\infty = 3.48$).

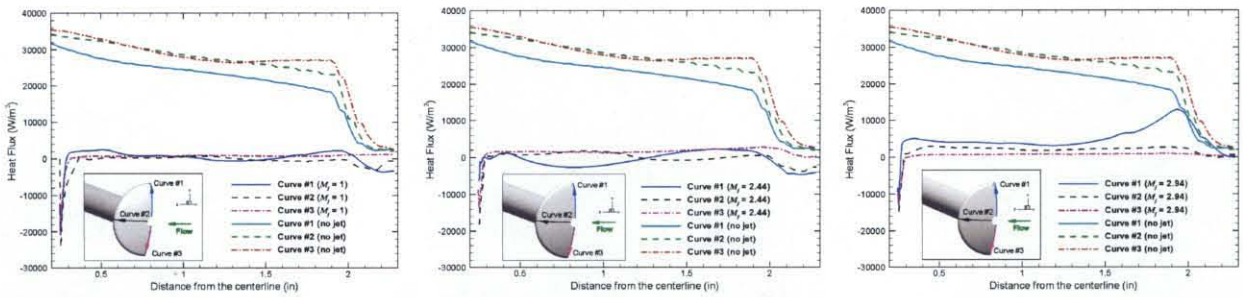

Figure 27. Comparisons of heat flux distributions at capsule face with and without counterflowing jet ($M_\infty = 3.48$, $\alpha = 10$, $\dot{m}_j = 1$ lb/s).

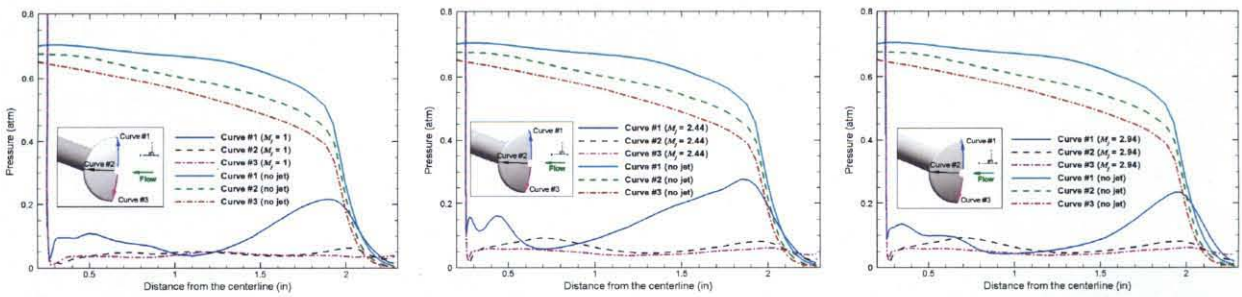

Figure 28. Comparisons of pressure distributions at capsule face with and without counterflowing jet ($M_\infty = 3.48$, $\alpha = 10$, $\dot{m}_j = 1$ lb/s).

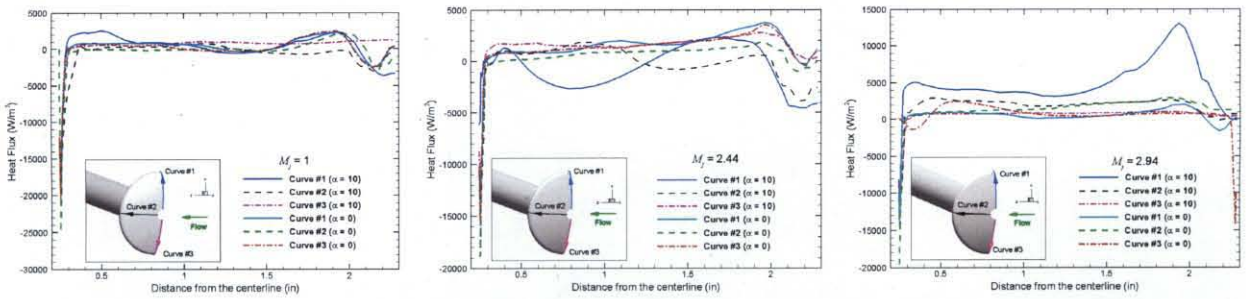

Figure 29. Comparisons of heat flux distributions at capsule face with different angles of attack (M_∞ = 3.48).

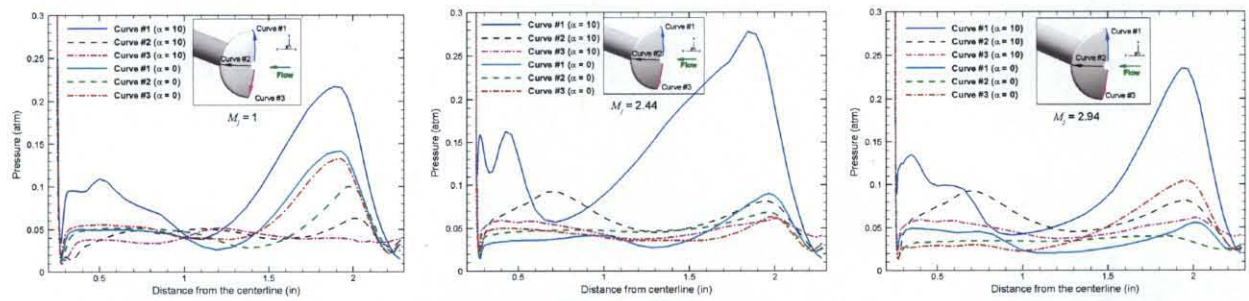

Figure 30. Comparisons of pressure distributions at capsule face with different angles of attack (M_∞ = 3.48).

			Drag force (N)	Lift force (N)	Heat flux (W/m^2)
M_∞ = 3.48	α = 0	M_j = 0	217.2	0	340 ~ 19600
		M_j = 1	146±4	0	-25000 ~ 4700
		M_j = 2.44	165±8	0	-16000 ~ 3800
		M_j = 2.94	167±13	0	-19500 ~ 3000
	α = 10	M_j = 0	208	33	2100 ~ 35800
		M_j = 1	133.6±3	21.2±1.8	-24200 ~ 2600
		M_j = 2.44	157±14	27.6±3	-18000 ~ 2800
		M_j = 2.94	163±18	25.5±4	-15100 ~ 13000
M_∞ = 4.96	α = 0	M_j = 0	113.4 ~ 113.9	0	310 ~ 12500
		M_j = 1	133.9±2	0	-25300 ~ 1600
		M_j = 2.44	156±9.5	0	-18400 ~ 1700
		M_j = 2.94	157.5±3	0	-18500 ~ 1700
	α = 10	M_j = 0	108.5	16.9	650 ~ 27800
		M_j = 1	122.3±1.7	20.9±0.9	-24300 ~ 1200
		M_j = 2.44	140.3±3.7	23.6±0.7	-17000 ~ 3500
		M_j = 2.94	144.5±4.5	24.3±1	-18700 ~ 1800

Table 3: Summary of the predicted drag force and heat flux for $\dot{m}_j$ = 1 lb/s.

V. Conclusions

In the present study, the effect of the counterflowing jet on the aerothermodynamic environment around an Apollo-type capsule has been systematically analyzed. The cases simulated include two different freestream Mach numbers and two angles of attack with and without a counterflowing jet. There were three different nozzles with six different mass flow rates for the counterflowing jet. The results show that 1) the use of different counterflowing jet flow rate has a strong influence on the reduction of the pressure and heat flux at the capsule face, 2) the shock-jet interaction can switch between the short and long penetration modes depending on the jet flow rates, 3) the jet mass flow rate for which LPM occurs varies slightly with the counterflowing jet nozzles, 4) the counterflowing jet nozzle at a given flow rate has a weak effect on the flow around the capsule, 5) different freestream Mach numbers have similar flow characteristics with different levels of pressure and heat loads on the capsule, and 6) the angle of attack induces much higher pressures and heat loads on the windward side of the capsule. The comparisons with the test data reveal that the shock stand-off distance predicted by the employed CFD model agree relatively well with the test data, except in the case where the freestream Mach number is 3.48, jet Mach number is 1, and jet mass flow rate is 0.1 lb/s. Furthermore, the non-monotonic variations of the pressure and heat flux at the capsule face with respect to different jet flow rates are captured by the CFD simulations. However, the magnitude of pressure at the capsule face is under-predicted while the heat flux level is over-predicted. Despite the suspicion of the compressibility effect on turbulent jet mixing and the use of temperature boundary conditions, the numerical accuracy of the CFD model needs to be further validated, and the validity of the test data should be assessed to obtain it uncertainty. Overall, both the experimental and numerical studies demonstrate that the use of a counterflowing jet is a feasible approach to reduce the pressure and heat load on the capsule under an extreme environment such as the re-entry condition. Further investigations of experimental tests and numerical simulations under conditions closely resembling actual flight conditions during re-entry are needed so that more meaningful data can be provided to support the design the thermal protection system of the re-entry vehicle.

Acknowledgments

This study was partially supported by the Innovative Partnership Program Office at NASA Marshall Space Flight Center, through a Phase III Small Business Innovative Research contract with Engineering Sciences, Inc. The authors would like to thank Dr. Chau-Lyan Chang of NASA Langley Research Center for conducting some 2-D simulations using his CE-SE CFD code (EZ4D) to verify the frequency of the unsteady flow calculated in this study.

References

[1]Daso, E.O., Pritchett, V.E., Wang, T.S., Ota, D.K., Blankson, I.M., and Auslender, A.H., "The Dynamics of Shock Dispersion and Interactions in Supersonic Freestreams with Counterflowing Jets," AIAA Paper 2007-1423, 45th AIAA Aerospace Sciences Meeting and Exhibit, Reno, NV, Jan. 2007.

[2]Daso, E.O., Beaulieu, W., and Hager, J.O., "Prediction of Drag Reduction in Supersonic and Hypersonic Flows with Counter-flow Jets," AIAA Paper 2002-5115, 2002.

[3]Gilinsky, M., Washington, C., Blankson, I.M., and Shvets, A.I, "Spike-Nosed Bodies and Forward Injected Jets in Supersonic Flow," AIAA Paper 2002-3918, 2002.

[4]Josyula, E., Pinney, M., and Blake, W.B., "Applications of a Counterflow Drag Reduction Technique in High Speed Systems," AIAA Paper 2001-2437, June 2001.

[5]Jarvinen, P.O., and Adams, R.H., "The Effects of Retrorockets on the Aerodynamic Characteristics of Conical Aeroshell Planetary Entry Vehicles," AIAA Paper 70-219, January 1970.

[6]McGhee, R.J., "Effects of a Retrorockets Located at the Apex of a 140° Blunt Cone at Mach Numbers of 3.00, 4.50 and 6.00," NASA TN D-6002, January 1971.

[7]Chen, Y.S., "An Unstructured Finite Volume Method for Viscous Flow Computations", 7th International Conference on Finite Element Methods in Flow Problems, University of Alabama in Huntsville, Huntsville, Alabama, Feb. 3-7, 1989.

[8]Shang, H.M., Shih, M.H., Chen, Y.S., and Liaw, P., "Flow Calculation on Unstructured Grids with a Pressure-Based Method," Proceedings of 6th International Symposium on Computational Fluid Dynamics, Lake Tahoe, NV, Sep. 4-8, 1995.

[9]Chen. Y.-S., Zhang S., and Liu, J., "Stage Separation Performance Analysis Project," Final Report, H-34345D, Engineering Sciences, Inc., Huntsville, AL, 2002.

[10]Launder, B.E. and Spalding, D.B., "The Numerical Calculation of Turbulent Flows," *Computer Methods in Applied Mechanics and Engineering*, Vol. 3(2) , 1974, pp. 269-289.

[11]Chen, Y.-S., and Kim, S. W., "Computation of Turbulent Flows Using an Extended k-ε Turbulence Closure Model," NASA CR-179204, 1987.

[12]Liakopoulos, A., "Explicit Representations of the Complete Velocity Profile in a Turbulent Boundary Layer," *AIAA Journal*, Vol. 22, No. 6, 1984, pp. 844-846.

[13]Viegas, J.R., Rubesin, M.W., and Horstman, C.C., "On the Use of Wall Function as Boundary Conditions for Two-Dimensional Separated Compressible Flows," AIAA Paper 85-0180, AIAA 23rd Aerospace Sciences Meeting, Jan. 14-17, 1985.

[14]Karki, K.C., and Patankar, S.V., "Pressure Based Calculation Procedure for Viscous Flows at all Speeds in Arbitrary Configurations," AIAA J., Vol. 27, 1989, pp. 1167-1174.

[15]Patankar, S.V., *Numerical Heat Transfer and Fluid Flow*, Hemisphere, New York, 1980.

[16]Barth, T.J., and Jespersen, D.C., "The Design and Application of Upwind Schemes on Unstructured Meshes," AIAA Paper 89-0366, 1989.

[17]Rhie, C.M. and Chow, W.L., "A Numerical Study of the Turbulent Flow past an Isolated Airfoil with Trailing Edge Separation," *AIAA Journal*, Vol. 21, 1983, pp. 1525-1532.

[18]Van Der Vorst, H.A., "Bi-CGSTAB: A Fast and Smoothly Converging Variant of Bi-CG for the Solution of Nonsymmetric Linear Systems," *SIAM J. Sci. Stat. Comput.*, Vol. 13(2), 1992, pp. 631-644.

[19]Saad, Y. and Schultz, M.H., "GMRES: A Generalized Minimal Residual Algorithm for Solving Nonsymmetric Linear Systems," *SIAM J. Sci. Stat. Comput.*, Vol. 7(3), 1986, pp. 856-869.

[20]Raw, M., "Robustness of Coupled Algebric Multigrid for the Navier-Stkoes Equations," AIAA Paper 96-0297, 1996.

[21]Gropp, W., Lusk, E., and Skjellum, A., "*Using MPI*", MIT Press, ISBN 0-262-57104-8.

[22]Karypis, G. and Kumar, V., "METIS, A Software Package for Partitioning Unstructured Graphs, Partitioning Meshes, and Computing Fill-Reducing Orderings of Sparse Matrices," Version 3.0.3, November 5, 1997.

[23]Chen, Y.S., Shang, H.M., and Liaw, P., "A Fast Algorithm for Transient All-Speed Flows and Finite-Rate Chemistry," AIAA Paper 96-4445, 1996 AIAA Space Programs and Technologies Conference, September 24-26, 1996.

[24]Wang, T.S., Canabal, F., Cheng, G.C., and Chen, Y.S., "Multiphysics Analysis of a Solid-Core Nuclear Thermal Engine Thrust Chamber," AIAA Paper 2006-2927, 9th AIAA/ASME Joint Thermophysics and Heat Transfer Conference, June 5-8, 2006.

[25]Cheng, G.C., Ito, Y., Ross, D.H, Chen, Y.S., and Wang, T.S., "Numerical Simulations of Single Flow Element in a Nuclear Thermal Thrust Chamber," AIAA Paper 2007-4143, 39th AIAA Thermophysics Conference, June 25-28, 2007.

[26]Sarkar, S., Erlebacher, G., Hussaini, M.Y., and Kreiss, H.O., "The Analysis and Modeling of Dilatational Terms in Compressible Turbulence," NASA CR-181959, 1989.

[27]Speziale, C.G., Abid, R., and Anderson, E.C., "A Critical Evaluation of Two-Equation Models for Near Wall Turbulence," AIAA Paper 90-1481, 1990.

[28]Cheng, G.C., Farmer, R.C., and Chen, Y.S., "Numerical Study of Turbulent Flows with Compressibility Effects and Chemical Reactions," AIAA Paper 94-2026, 6th AIAA/ASME Joint Thermophysics and Heat Transfer Conference, June 20-23, 1994.